A Ray-Based Channel Modeling Approach for MIMO Troposcatter Beyond-Line-of-Sight (b-LoS) Communications

Ergin Dinc, *Student Member, IEEE*, and Ozgur B. Akan, *Senior Member, IEEE*

***Abstract*—Troposcatter can be used as a communication medium for beyond-Line-of-Sight (b-LoS) links. However, available troposcatter channel models do not provide comprehensive channel modeling especially at high frequencies. Therefore, the main motivation of this study is to develop a ray-based MIMO troposcatter channel model to analyze transmission-loss characteristics, coherence bandwidth and correlation between antennas for the first time in the literature for troposcatter communications. In addition, the link budget calculations and the distribution of capacity in troposcatter links are provided by using real world water vapor mixing ratio measurements.**

***Index Terms*—Electromagnetic scattering, communication channels, propagation, MIMO systems, atmospheric measurements.**

I. Introduction

TROPOSCATTER, that is also known as tropospheric scatter, is the scattering of the propagating signals due to the imperfections in the troposphere. Most of the scattered power is directed in the direction of the incoming ray. However, some portion of the scattered signals can be received at the receiver side by pointing the transmitter and receiver antennas to the radio horizon as in Fig. 1. The intersection of the beam-widths of the antennas forms the troposcatter common volume where the scattered signals can be directed to the receiver. In this way, the scattering effect can be utilized as communication medium for b-LoS links up to 300 km between 1–10 GHz, and the modern troposcatter equipments are mostly focus on 4.4–5 GHz frequency spectrum [1].

In the past, troposcatter communication was widely used for both civilian and military b-LoS applications. However, due to very large antenna sizes and high transmission-losses, troposcatter applications were replaced by Satellite Communications (SATCOM). On the other hand, SATCOM has intrinsic limitations due to the excessive transmission delays and capacity problems at regions having low satellite coverage. Therefore, b-LoS communication requires alternative techniques especially for the military applications. HF frequency applications or relay nodes can be preferable for the b-LoS communications. However, HF frequency applications are band-limited in their nature, and relay nodes can be exposed to hostile attacks. For these reasons, troposcatter communication stands as a promising candidate for b-LoS communications with the advancements in the troposcatter equipment and communication techniques. Available state-of-the-art solid-state amplifiers and troposcatter modems can reach up to 2 kW and 22 Mbps, respectively [2], [3]. Thus, troposcatter systems can be used in b-LoS links requiring high data rates especially with the employment of multiple-input-multiple-output (MIMO) systems.

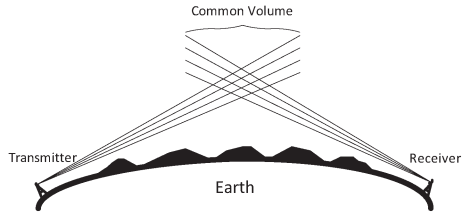

Fig. 1. Troposcatter b-LoS paths.

To evaluate the performance of the troposcatter systems, it is required to investigate the characteristics of the troposcatter channel. However, the available troposcatter channel models are inefficient to model the complex and time-varying air turbulence [4]–[8]. Therefore, we have introduced a ray-based troposcatter channel modeling approach in our preliminary work [9]. In our approach, the beam-width of each antenna is divided into small parts, and transmission-loss calculations are performed for each ray to estimate power delay spectrum (PDS) of the channel. We introduce the differential scattering cross-section calculations by combining the available scattering studies [10], [11] and the meteorological refractive index structure constant studies [12]. With this approach, we are capable of utilizing the real world water vapor mixing ratio measurements conducted by NASA [13] to consider atmospheric changes. In our preliminary work [9], this approach is proposed and simulated for different instantaneous bandwidths to show that troposcatter systems can achieve high data rates. In this paper, we further extend our approach and analysis to derive the coherence bandwidth, RMS delay spread and correlation between vertically spaced antennas for the first time in the literature.

The main contributions of this paper are four-fold. Firstly, we extend our proposed ray-based approach for realistic b-LoS troposcatter path geometries which considers antenna height

Manuscript received July 28, 2014; revised October 31, 2014 and January 20, 2015; accepted March 18, 2015. Date of publication March 26, 2015; date of current version May 14, 2015. A preliminary version of this work was presented in IEEE PIMRC'13. The associate editor coordinating the review of this paper and approving it for publication was B. Clerckx.

The authors are with the Next-generation and Wireless Communications Laboratory, Department of Electrical and Electronics Engineering, Koc University, Istanbul, 34450 Turkey (e-mail: edinc@ku.edu.tr; akan@ku.edu.tr).

Color versions of one or more of the figures in this paper are available online at http://ieeexplore.ieee.org.

Digital Object Identifier 10.1109/TCOMM.2015.2416716

and obstacles in the communication path. Secondly, the results of our proposed approach are compared with the ITU-R's empirical model for predicting annual and seasonal transmission losses in the troposcatter links [5] for verification. In addition, we provide link budget calculations for high frequency troposcatter systems. Thirdly, the coherence bandwidth and RMS delay spread of the channel are derived to estimate the fading behavior of the channel for given channel parameters for the first time in the literature. Lastly, we introduce vertical diversity and analyze the correlation between vertically spaced antennas for the first time. The simulation results are presented for the capacity of the MIMO troposcatter links by using real world measurements and our proposed ray-based approach.

The remainder of the paper is organized as follows. Section II presents the related work. Section III provides troposcatter channel geometry. In Section IV, troposcatter transmission-loss calculations are introduced. In Section V, we provide the comparison of the ITU-R's model and our approach and link budget calculations. Section VI includes coherence bandwidth and RMS delay spread results. In Section VII, the correlation between vertically spaced antennas is analyzed and capacity results are presented in Section VIII. Lastly, the conclusions are presented in Section IX.

II. Related Work

Available troposcatter studies generally focus on the prediction of the annual and the worst month transmission-losses with statistical methods [4], [5]. Although these statistical methods can capture the seasonal changes in the channel, fast variations and non-homogeneities in the channel cannot be modeled with such statistical approaches. In addition, [6] provided analytical expression for PDS of the troposcatter links. The analytical studies show that the envelope of PDS obeys the Rayleigh distribution. In addition, there exists some experimental studies [14], [15]. In [15], the correlation between vertically spaced antennas are presented with real world measurements, and the distribution of the fading in the troposcatter channel is reported as *Rayleigh*. Based on the analytical and experimental studies, there are also some studies that focus on the performance metrics in the troposcatter channels [7], [8], [16].

In the available analytical studies, the scattering is modeled only with the scattering angle [6]. For this reason, these models are inefficient to derive PDS, coherence bandwidth, and RMS delay spread which show significant dependence on the channel conditions. To this end, the main motivation of our work is to develop a comprehensive MIMO troposcatter channel modeling approach which considers the fluctuations and non-homogeneities in the air turbulence.

In our approach, the troposcatter is modeled with Rayleigh scattering approximation [10]. Since the scattering particles in the troposphere is much smaller than the wavelength of the signals, Rayleigh scattering approximation is valid for the troposcatter. To model the atmospheric turbulence, there are three major techniques: Booker-Gordon, Gaussian model and Kolmogorov spectrum technique. Booker-Gordon method uses variance in the exponential correlation however, the correlation is based on mathematics not the physics [10]. Furthermore, Gaussian model uses Gaussian correlation function. Therefore, these two models cannot effectively explain the troposcatter. However, Kolmogorov spectrum technique is based on the actual turbulence characteristics and it assumes the existence of locally homogeneous medium within the outer scale turbulence. Thus, this technique allows us to model the atmospheric changes with the real world water vapor mixing ratio measurements [13] in Section IV.

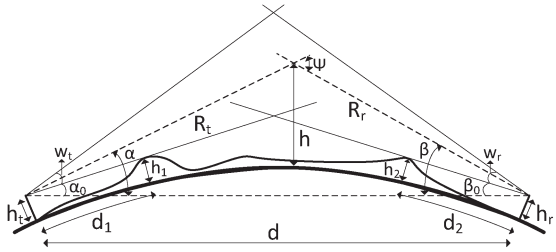

Fig. 2. The geometry of the troposcatter link.

TABLE I
The Parameters in Troposcatter Geometry

d	*Distance between TX/RX*
$h_{t,r}$	*Height of TX/RX*
$h_{1,2}$	*Height of obstacles*
$d_{1,2}$	*Distance between obstacle to TX/RX*
$R_{t,r}$	*Distance between scatter point and TX/RX*
α_0, β_0	*Beam elevation above horizontal line at TX/RX*
α, β	*Instantaneous beam elevation of the ray above horizon at TX/RX*
Ψ	*Scatter angle*
$w_{t,r}$	*Beam-width of the TX/RX*

III. Troposcatter Geometry

In [9], we have utilized simple channel geometry which assumes that both of the antennas are placed on the ground. In this paper, we extend this channel model to include the effects of antenna heights and obstacles in the b-LoS links.

Troposcatter channel geometry can be seen in Fig. 2 and the description of the parameters that are used in Fig. 2 can be found in Table I. The remainder of the section covers the investigation of beam elevations and path length calculations.

A. Beam Elevations Above Horizon

We define elevation angles with respect to horizontal line between transmitter and receiver (denoted as horizon). Instead of antenna elevation angles, we use *beam elevation* that is the elevation of the antenna beam with respect to horizon (α_0, β_0). The proposed model divides the 3 dB beam-width of the antennas to small parts and calculates path lengths separately for each ray.

Beam elevations of the antennas are critical in the troposcatter systems. Even 1° increase in the elevation angle can result in 9 dB decrease in the received power due to both increase in the path lengths and increase in the height of the common volume [14]. As the beam elevations increase, the path lengths becomes longer and this effect results in higher transmission-loss. In the same way, increase in the beam elevations cause increase in the height of the common volume. Upper parts of atmosphere

has less scatterers such as hydro-meteors. Therefore, the beam elevations should be as low as possible to achieve higher received powers.

In Fig. 2, beam elevations also depend on the obstacles in the path and the lowest angle which cannot be blocked by any obstacle is called as *radio horizon*. Elevation angle of the antennas with respect to radio horizon is given as [4]

$$\theta_1 = h_1 - h_t/d_1 - d_1/(2R_0), \tag{1}$$

$$\theta_2 = h_2 - h_r/d_2 - d_2/(2R_0), \tag{2}$$

where R_0 represents the effective radius of the earth. Since low elevation angles are used in troposcatter systems, the curvature of the earth becomes important and the effective radius of the earth is given as

$$R_0 = k_e R_e \text{ km}, \tag{3}$$

where R_e is the earth radius ($\approx$ 6370 km) and k_e represents the effective earth radius factor. Instead of using a median value for k as in [9], we calculate this parameter for real world conditions. The effective earth radius factor is given as [17]

$$k_e = 157/(157 - \Delta N), \tag{4}$$

where ΔN (N-units/km) is the average radio-refractive index lapse-rate through the lowest 1 km of the atmosphere and this value is derived by using real world data sets [13] in Section IV-B. The resulting ΔN is calculated as 46 N-units/km on the average for a day in August [13]. By considering the monthly average value of 50 N-units/km that is provided by ITU-R for the same site at the same month [18], we can conclude that our calculations are consistent with the empirical results.

The beam elevations with respect to horizon for the minimum path lengths are found as [4]

$$\alpha_0 = \theta_1 + d/dR_0 + (h_1 - h_2)/d, \tag{5}$$

$$\beta_0 = \theta_2 + d/dR_0 - (h_1 - h_2)/d. \tag{6}$$

The resulting instantaneous beam elevation angles above horizon α, β (dashed lines in Fig. 2) can be found by $\alpha = \alpha_0 + \Delta w$ where $\alpha_0 < \alpha < \alpha_0 + w_t$ and $\beta = \beta_0 + \Delta w$ where $\beta_0 < \beta < \beta_0 + w_r$. In our model, $1/\Delta w$ number of rays launch from the antennas to estimate PDS of the channel.

B. Path Lengths

The distance between the scattering point and transmitter/receiver ($R_{t,r}$) is calculated with the following relationship

$$d/\sin(\Psi) = R_t/\sin(\beta) = R_r/\sin(\alpha), \tag{7}$$

where the scattering angle is given by $\Psi = \alpha + \beta$. By using (7), the total path length is given by $L = R_t + R_r$.

To find the delay spread of each ray, the difference between L and a reference path is required. Since troposcatter communication has no line-of-sight (LOS) component, the shortest path which is associated with the lowest possible beam elevation angles (α_0 and β_0) is assumed as the reference path. Therefore, the path length difference between the reference path and instantaneous path is used for delay calculations and formulated as [4]

$$\Delta d = L - d_0 = \frac{d}{2}(\alpha\beta - \alpha_0\beta_0) \text{ km}. \tag{8}$$

The delay spread of the reference path is assumed as the excess delay of the channel.

IV. Troposcatter Transmission-Loss

We introduce the differential transmission-loss calculations to estimate the PDS, coherence bandwidth and RMS delay spread of the troposcatter channel by using real world measurements. This section provides the scattering cross-section model and the differential radar range equation calculations for the troposcatter channel.

A. Scattering Cross-Section

Scattering cross-section represents the area in which the propagating waves can be scattered and depends on the wavelength of the rays, permittivity and most importantly the size and distribution of the scattering particles. Therefore, the variations in the air turbulence are modeled via scattering cross-section in the proposed approach. We utilize the existing scattering cross-section studies [10], [11] to derive differential scattering cross-section. In addition, we combine the scattering studies with the meteorological structure constant of the index of refraction studies [12] to utilize real world measurements [13] for the first time in the literature.

The sizes of the scattering particles with respect to the wavelengths are critical because the type of the dominant scattering depends on this relationship. We model the clear air turbulence within this study. Therefore, the sizes of the scatterers in the troposcatter links are generally in the order of 1–10 μm whereas high frequency troposcatter systems is expected to use carrier frequencies between 1–10 GHz (wavelengths between 30–300 mm). Therefore, the wavelengths of the signals are much larger compared to the scattering particles. In such scenarios, the Rayleigh scattering approximation is valid for the scattering and it assumes that the electrical fields inside the scattering particles form constant vectors [10].

By using the Rayleigh scattering approximation, the differential scattering cross-section is found in Appendix A as

$$\sigma_V(\alpha, \beta, n) = 2\pi k^4 \cos(\Psi)^2 \Phi(\alpha, \beta, n) \text{ m}^2, \tag{9}$$

where $k = 2\pi/\lambda$ is the wavenumber and the fourth power dependence of the wavenumber comes from Rayleigh scattering approximation. Φ is the turbulence spectrum which is modeled with Kolmogorov theory [10]. Dependencies of parameters are included in formulas. α and β show dependency on the geometry, and n represents any dependency on the refractivity index and its gradient.

In the Kolmogorov spectrum technique, the clear air atmospheric turbulence is modeled via the turbulence eddies:

the outer scale (Eddy size$> L_0$), and the inner scale turbulences ($L_0 >$ Eddy size $> l_0$). The outer scale turbulence is anisotropic according to the climate conditions, and it is caused by the wind shear or the temperature gradient. In addition, the inner scale turbulence is the inertial range where the turbulence is assumed as isotropic and it defines the dissipation range. For the inner scale turbulences, the turbulence is isotropic and the energy of the eddies dominates the spectrum [10]. Therefore, the spectrum is proportional with $\Phi(k_s) \approx k_s^{(-11/3)}$, where $k_s = 2k\sin(\Psi/2)$. The microwave propagation is mostly affected by the inner scale turbulence [19], and the resulting Kolmogorov spectrum is formulated as [10]

$$\Phi(\alpha, \beta, n) = 0.033 C_n^2 \left(2k\sin(\Psi/2)\right)^{-11/3} \text{ m}^3, \tag{10}$$

where C_n^2 represents the structure constant of the index of refraction and it depends on both the height and refractivity gradient. C_n^2 is given as [12]

$$C_n^2 = 2.8 \left(\frac{\partial n}{\partial z}\right)^2 L_0(z)^{4/3}, \tag{11}$$

where n represents the index of refraction, and z represents the height. L_0 is the outer scale of the turbulence that represents the distance in which the atmosphere can be assumed as homogeneous. The values of the L_0 may vary a few meters to 100 m as suggested in [19]–[21] which is based on millimeter-wave measurements. Therefore, we model the outer scale of the turbulence as a uniform random variable between 3–100 m as in [20] which consider earth to satellite links.

B. Refractivity Calculations

We calculate C_n^2 by using both real world water vapor mixing ratio measurements that are provided by NASA Langley Research Center [13] and the ITU-R refractivity model which estimates the average refractivity profile of the troposphere [18]. We utilize the real world measurements to verify our model for a specific climate region, and the ITU-R's model is also utilized to show that the proposed method is able to predict the transmission-losses in other climate types as well.

1) With Real World Data Set: One of the main contributions of our approach is the utilization of the real world water vapor mixing ratio measurements [13] because the proposed technique can take real world measurements as input instead of the statistical methods [7], [8]. Since C_n^2 depends on the index of refraction, we first find the vertical refractivity profile based on water vapor mixing ratio measurements. The fluctuations in the index of refraction is calculated using the simple relationship between them [18]

$$N = (n-1) \times 10^6,$$
$$\frac{\partial N}{\partial z} = \frac{\partial n}{\partial z} \times 10^6 \text{ N-units/m}. \tag{12}$$

For microwave frequencies, the refractivity of the air is formulated as [18]

$$N = \frac{77.6}{T}(P + 4810 \times e/T) \text{ N-units}, \tag{13}$$

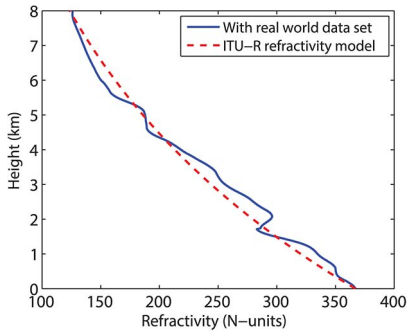

Fig. 3. The refractivity profiles with the dataset and ITU-R model [18].

where P represents total atmospheric pressure in mb, T represents the temperature of the air in Kelvin and, e represents vapor pressure that can be represented as

$$e = \frac{P}{\varepsilon}\omega \text{ mb}, \tag{14}$$

where ω represents the water vapor mixing ratio of the air that is the amount of water in air in g/kg. ω is directly taken from height dependent measurements. The molecular mass ratio of water vapor to air (ε) is taken as 0.622 [22].

By using (11), (13) and (14), the C_n^2 is calculated as 5.20×10^{-14} m$^{-2/3}$ on the average at the heights of troposcatter common volume (600–2300 m) for the parameters that we used in this paper. In addition, the datasets that we use in this paper were measured in the western coastal part of Africa, near Cape Verde Islands in August [13] mostly afternoon hours. However, the ground level values for C_n^2 is calculated as 3.08×10^{-12} m$^{-2/3}$ and similar values can be found in [23] and [21] for different sites. Furthermore, [20], [24] also show the vertical change in C_n^2, and our average results quite agree with the results provided in [20], [24].

In this study, we consider the clear air atmospheric turbulence under standard atmospheric conditions. Therefore, we do not consider the effects of the atmospheric ducts. We also analyze the generated vertical refractivity profiles to detect any kind of duct formations. According to analysis, we do not observe any duct formation for the used data set [13]. However, the presence of atmospheric ducts may cause power loss due to its trapping effects [25].

2) With ITU-R Model: With the ITU-R refractivity model [18], the reference refractivity of the atmosphere can be calculated as

$$N = N_0 \exp(-z/z_0), \tag{15}$$

where z is the height in m, N_0 is the average value of the atmospheric refractivity at sea level in N-units, and z_0 is the scale height in m. [18] provides the average values for the N_0 for 5-year data set, but only one value is specified for z_0 as 9.5 km. Since [13] were measured in the western coastal part of Africa, we select N_0 values for the same region as well. Therefore, the result of the ITU-R refractivity model [18] will have less accuracy to model the atmospheric turbulence.

Fig. 3 presents sample refractivity results that are calculated with the real world data set and ITU-R model. As noticed, the ITU-R model is just the reference curve for the refractivity.

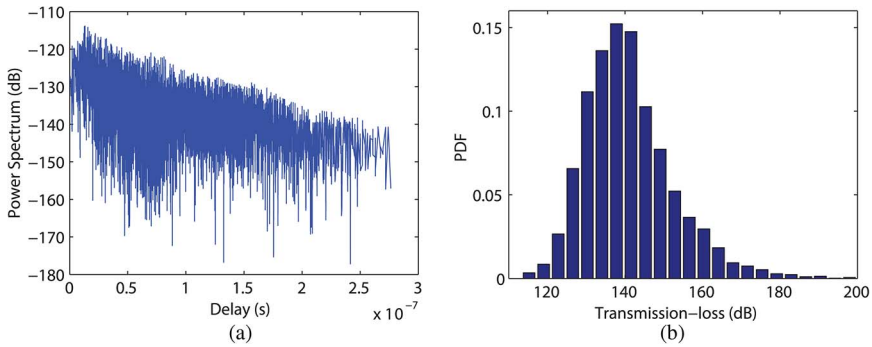

Fig. 4. (a) PDS spectrum and, (b) histogram of multipath components for a 150 km troposcatter link for 4.7 GHz.

However, both curves becomes closer after 3 km. For this reason, we utilize the ITU-R refractivity model to generate the transmission-loss results for high ranges in Section V-A because the high ranges form high troposcatter common volumes where the ITU-R model can give reasonable results for the refractivity of the troposphere.

C. The Radar Range Equation

Since the transmission-loss of each ray is calculated separately with the proposed ray-based approach, we define differential bistatic radar range equation as

$$P_r(\alpha,\beta,n) = \int_{dV_c} \frac{P_t G_t G_r \sigma_V(\alpha,\beta,n)\lambda^2 \varrho}{(4\pi)^3 R_t(\alpha,\beta)^2 R_r(\alpha,\beta)^2} dV, \quad (16)$$

where P_t is transmit power, G_t and G_r are antenna gains for transmitter and receiver, respectively. ϱ represents polarization mismatch factor which is used directly as introduced in [9]. Since the parameters such as range, obstacle height and frequency are fixed in the differential calculations, P_r is shown only as a function of geometry and refractive index. dV_c is differential scattering volume which is given as

$$dV_c(\alpha,\beta) = \frac{R_r^2 R_t^2 (dw)^2}{\sqrt{R_r^2 + R_t^2}\sin(\Psi)} \text{ m}^3, \quad (17)$$

where dw is the differential beam-width of the ray.

The Kolmogorov spectrum assumes that the atmospheric turbulence as locally locally homogeneous. Therefore, the scattering cross-section is assumed constant for the scattering volume dV_c, and the differential bistatic radar range equation is simplified as

$$P_r(\alpha,\beta,n) = \frac{P_t G_t G_r \sigma_V(\alpha,\beta,n) dV_c(\alpha,\beta)\lambda^2 \varrho}{(4\pi)^3 R_t(\alpha,\beta)^2 R_r(\alpha,\beta)^2} \text{ W}. \quad (18)$$

By combining (9)–(11), (17), and (18) we derive the bistatic equation as

$$P_r(\alpha,\beta,n) = \frac{P_t G_t G_r \pi^2 dw^2 \cos(\Psi)^2 \left(\frac{\partial n}{\partial z}\right)^2 L_0(z)^{4/3} \varrho}{21.64\lambda^2 \sqrt{R_r^2 + R_t^2}\sin(\Psi)(2k\sin(\Psi/2))^{11/3}} \text{ W}, \quad (19)$$

where $\partial n/\partial z$ is directly calculated by using the real world measurements. $\sqrt{R_r^2 + R_t^2}$ term shows the linear relationship between the range and the transmission-loss. The same result also appears in the ITU-R's empirical model [5].

D. Simulation Results

PDS of the channel can be generated by using our ray-based approach. Fig. 4 presents both PDS, and transmission-loss (P_r/P_t) distribution of multipath components for a measurement instant with the following channel parameters: $f = 4.7$ GHz, $d = 150$ km, $h_{t,r} = 27$ m, $h_{1,2} = 41$ m, $d_{1,2} = 21$ km and $G_{t,r} = 41.5$ dB. According to Fig. 4(b), the distribution of the transmission-loss of the multipath components is close to Rayleigh distribution. This result is mentioned in [6]–[8], [15], but it was never quantitatively shown. In this work, we derive this conclusion quantitatively for the real world conditions for the first time in the literature.

V. Transmission-Loss and Link Budget Calculations

To verify our ray-based approach, we utilize ITU-R P.617 annual and average transmission-loss prediction method which is introduced in [5]. In [5], ITU-R provides the empirical model for predicting transmission-loss values for non-exceedance percentages of the time. The equation and parameters of the ITU-R's model show changes according to climate zones such as dry, tropical, etc. The real world datasets that we are using were measured in the western coastal part of Africa, near Cape Verde Islands in August [13]. According to the climate map in [5], the data set that we are using is in category 3 (dry climate). Therefore, we use the equations and parameters for category 3 while calculating the transmission-loss values by using ITU-R P.617. In addition, we provide link budget calculations for the troposcatter links.

A. Comparison of Our Model and ITU-R's Model

To find the transmission-loss results with our proposed approach, the transmission-loss of the link is calculated for each measurement instant. There are 1000 measurement instants that are measured in August near Cape Verde Islands [13]. The average of these transmission-loss values for different times is denoted as the transmission-loss of the link for a given range. Since ITU-R's model is most accurate below 5 GHz, we compare the results only for 4.7 GHz link with respect to range. The following channel parameters are utilized in the simulations: $h_{t,r} = 27$ m, $h_{1,2} = 41$ m, $d_{1,2} = 21$ km and

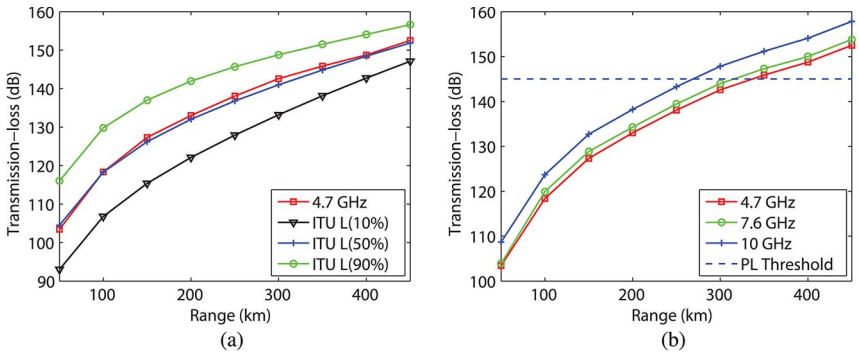

Fig. 5. Transmission-loss vs. range (a) Comparison of our model and ITU-R's model for 4.7 GHz, (b) Transmission-loss for different frequencies.

TABLE II
THE COMPARISON OF TRANSMISSION-LOSSES (dB) FOR ALL CLIMATE REGIONS

	Climates											
	1		2		3		4		5		6	
Range (km)	50%	*Our Model*	50%	*Our Model*	50%	*Our Model*	50%	*Our Model*	50%	*Our Model*	50%	*Our Model*
250	157.2	152.4	146.9	144.7	136.8	134	155.7	154.5	146.9	149.8	150.4	149.2
350	165.2	159.5	154.6	151.7	144.8	147.1	163.4	160.9	154.6	156.8	158.1	156.6
450	172.4	166.4	161.3	158.7	151.9	153.9	170.1	167.7	161.3	163.1	164.8	163.4

$G_{t,r} = 41.5$ dB. The maximum LoS range can be found with the generic formula $d_{LOS} < 4.12\sqrt{h_t} + 4.12\sqrt{h_r}$. With our channel parameters, LOS range can reach up to 42 km. Beyond this range is denoted as b-LoS range. Therefore, we focus on the ranges higher than 50 km in this subsection.

To verify our results, we compare the transmission-loss results of ITU-R's model and our proposed approach. We derive the PDS of the troposcatter channel by using troposcatter geometry and transmission-loss calculations introduced in Sections III and IV. In Fig. 5(a), the average of 1000 instants for each range and ITU-R's model for different non-exceedance percentages are presented. Since the transmission-loss results that are generated with our model are the average of the time instants, it is expected that our proposed approach should be close to the 50% not exceeded of the time. In Fig. 5(a), our model is very close to the 50% curve.

In addition, we compare our ray-based troposcatter channel modeling approach for other climate types by using ITU-R average refractivity calculations [18] as discussed in Section IV-B2. Since the refractivity profile is calculated with the average values, we only compare our results with the 50% non-exceeding rate as in Table II. As noticed, the 50% transmission-losses are quite consistent with our calculations. However, they do not show very close matching as in Fig. 5(a) because the refractivity estimations that are generated with [18] has some errors as shown in Section IV-B2, and we utilize only the average values not the site specific values. Thus, we can conclude that our proposed ray-based troposcatter channel modeling approach agrees with the empirical results [5].

B. Link Budget Calculations

To determine the maximum b-LoS communication range that can be provided by the troposcatter communication, we provide troposcatter link budget calculations by using our ray-based approach for $P_t = 60$ dBm, $G_{t,r} = 41.5$ dB, cable-losses $L_q = 5$ dB. For modern troposcatter equipments, the minimum received power should be -90 dBm [26], [27]. To satisfy the minimum of -90 dBm received power, the maximum transmission-loss is calculated as 145 dB. Fig. 5(b) shows the transmission-loss for different frequencies and the calculated 145 dB transmission-loss threshold (PL threshold). As noticed, 4.7 GHz can provide communication link up to 300 km. However, this transmission-losses are in the order of 50% not exceeded of the time as shown in Fig. 5(a). If we look at the losses in the Fig. 5(a), 4.7 GHz can achieve the communication 90% of the time up to 250 km. As a result, troposcatter communication can be used in b-LoS links up to 250 km with very high availability rates. Since high frequencies can achieve lower ranges, the utilization of lower frequencies is more preferable.

VI. COHERENCE BANDWIDTH AND RMS DELAY SPREAD

The fading characteristics of the channel is another important design constraint for the b-LoS troposcatter communications. We examine the coherence bandwidth and RMS delay spread of the channel to determine whether the selected bandwidth experiences flat fading or frequency selective fading according to the channel conditions.

Fig. 6(a) presents the coherence bandwidth vs. range for different carrier frequencies for the following channel parameters: $h_{t,r} = 27$ m, $h_{1,2} = 41$ m, $d_{1,2} = 21$ km, $G_{t,r} = 41.5$ dB, $D_{ant} = 3$ m and $P_t = 1000$ W. Here, there is a direct relationship between carrier frequency and coherence bandwidth of the channel because the beam-width of the parabolic reflector antennas depend on the frequency, i.e., $w_t = w_r = 70\lambda/D_{ant}$, where D_{ant} is the antenna diameter. The same effect can be seen in RMS delay spread results that are presented in Fig. 6(b). Since the decreasing beam-width of the antennas

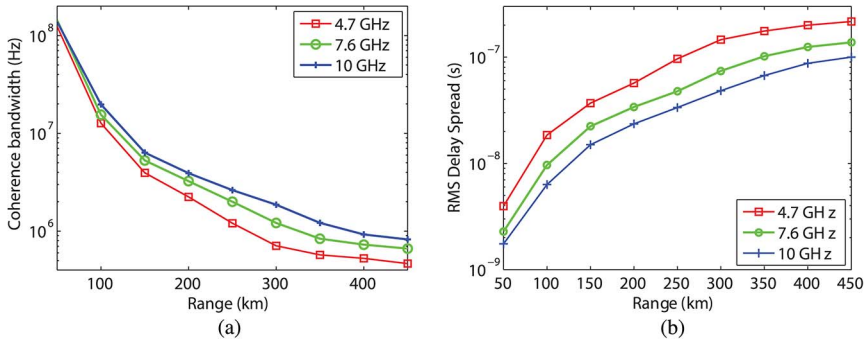

Fig. 6. (a) Coherence bandwidth and, (b) RMS delay spread of troposcatter link vs. range.

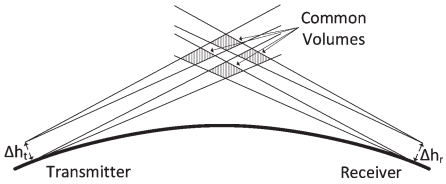

Fig. 7. The geometry of the vertical diversity in troposcatter.

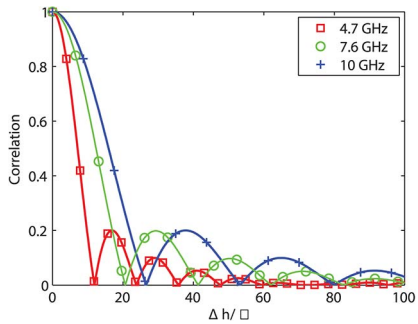

Fig. 8. Correlation vs. vertical height difference for receiver.

decreases the troposcatter common volume, the delay spread of the channel becomes less. According to these results, 150 km b-LoS troposcatter link has ≈ 4 MHz coherence bandwidth and $\approx 1.85 \times 10^{-8}$ s RMS delay spread for 4.7 GHz. Therefore, 1 MHz bandwidth for 150 km link at 4.7 GHz experiences flat fading. However, at higher ranges the channel may become the frequency-selective and OFDM systems may be preferable to avoid frequency-selective effects of the channel.

VII. Vertical Diversity

Modern b-LoS communication requires reliability and high data rates. However, troposcatter introduces high losses due to the changes in the atmospheric conditions. Therefore, troposcatter b-LoS systems require the employment of MIMO systems to increase the reliability and the maximum data rate that can be provided. In this section, we investigate the utilization of vertically placed antennas and their correlations as a function of vertical distance between them.

2×2 vertical diversity provides four different common volumes as in Fig. 7 because increasing antenna heights decreases beam elevation of the antennas. However, the separation between antennas should be kept small for practical reasons. In this case, different common volumes will intersect with each other and this effect introduces correlation between vertically spaced antennas.

The employment of more receiver antennas than transmitters is more advantageous and common in modern systems. For this reason, we determine the correlation between receiver antennas by modifying our ray-based algorithm. We assume that transmitters are uncorrelated with enough spacing between them. To find the correlation between receivers, we exclude the effects of atmospheric profiles. Each ray is assumed to reach the receiver with the same power as in [28] because our main aim is to find the correlation between antennas which can be generalized for all climate conditions. Thus, ray powers between transmitter i and receiver j is calculated as

$$P_{ri,j}(\alpha,\beta) = \exp\left(-j\frac{2\pi}{\lambda}(R_{ti,j}(\alpha,\beta) + R_{ri,j}(\alpha,\beta))\right), \tag{20}$$

where $R_{ti,j}$ and $R_{ri,j}$ are the distances between the scattering point with transmitter i and receiver j. The resulting correlation $\rho_{k,l}$ between receivers k, l is found by the correlation between their PDSs.

Fig. 8 presents correlation vs. vertical separation ($\Delta h/\lambda$) in vertical diversity troposcatter systems. The increase in the carrier frequency increases the correlation at the same ratio. However, since the wavelength of the higher frequencies are lower, increase in the carrier frequency does not increase the required spacing for a given correlation value. To verify our results, we compare our results with the empirical recommendations provided by ITU-R [5]. The safe vertical spacing for antennas to be uncorrelated is given as [5]

$$\Delta h_v = 0.36(D_{ant}^2 + 4I_v^2)^{1/2}, \tag{21}$$

where D_{ant} is antenna diameter and I_v is the empirical scale length in vertical direction which can be taken as 15 m [5]. According to (21), the resulting spacing between antennas should be 10.85 m which is $170\Delta h/\lambda$ for 4.7 GHz. According to our results, the correlation is almost zero for $80\Delta h/\lambda$ and above for 4.7 GHz. ITU-R's empirical results give safe spacing between antennas to be uncorrelated. In addition, [15] provides some experimental correlation results for the vertical separations. According to their results, $10\lambda - 30\lambda$ separations provide uncorrelated receivers. Therefore, our vertical correlation

results are consistent with both the ITU-R's recommendation and experimental studies.

VIII. Capacity Results for Troposcatter Vertical Diversity

We investigate the performance of b-LoS troposcatter communication in terms of capacity to show that b-LoS troposcatter communication is suitable for high data rate applications. For this reason, this section first includes capacity formulations by using our approach and simulation results for MIMO troposcatter systems.

A. Capacity Formulation

The system use 1 MHz bandwidth for 4.7, 7.6 and 10 GHz carrier frequencies. For this bandwidth, the channel experiences flat-fading as described in Section VI. Flat-fading channel is modeled as

$$\mathbf{y} = \mathbf{H}\mathbf{x} + \mathbf{n}, \tag{22}$$

where $\mathbf{H}_{N_R \times N_T}$ is the channel gain matrix, where N_T and N_R are the number of transmitter and receiver antennas, respectively. $\mathbf{x}_{N_T \times 1}$ and $\mathbf{y}_{N_R \times 1}$ are transmitting and receiving vectors.

In our approach, the changes with time is modeled with real world measurements. We use channel matrix normalization to model the effect of large-scale transmission-loss that changes with time due to atmospheric effects. The large-scale transmission-loss is derived by using real world measurements as described in Section IV. Small-scale fading is assumed as Rayleigh fading as described in Section IV-D. Normalized channel gain matrix $\tilde{\mathbf{H}}$ is found as [29]

$$\tilde{\mathbf{H}} = \frac{\mathbf{H}}{\sqrt{\frac{1}{N_T N_R}\|\mathbf{H}\|_F^2}}, \tag{23}$$

where $\|.\|_F$ is the Frobenius norm.

We assume that there is no correlation between transmitters as analyzed in Section VII. With correlated receiver antennas, normalized channel gain matrix is modeled as [30]

$$\tilde{\mathbf{H}} = \left(\mathbf{R}_H^{RX}\right)^{1/2} \mathbf{G}, \tag{24}$$

where $\mathbf{G}$ is the complex Gaussian iid matrix. $(\mathbf{R}_H^{RX})^{1/2}$ is the root of the receiver antenna correlation matrix ($\mathbf{R}_H^{RX}$).

The resulting channel capacity matrix can be represented as [31]

$$C = \sum_{i=1}^{\min(N_T, N_R)} \log_2\left(1 + \frac{\gamma}{N_T}\lambda_i\right), \tag{25}$$

where λ_i are the nonzero eigenvalues of the Wishart matrix $\tilde{\mathbf{H}}\tilde{\mathbf{H}}^H$ for $N_R \leq N_T$ or $\tilde{\mathbf{H}}^H\tilde{\mathbf{H}}$ for $N_R > N_T$. $\gamma = SNR_{av}/N_T$, where the average SNR on the channel is found as [29], [32]

$$SNR_{av} = \frac{P_t}{\sigma_n^2 N_T N_R}\|\mathbf{H}\|_F^2, \tag{26}$$

where P_t is the transmit power, σ_n^2 is the noise power. The values for SNR_{av} is derived with our ray-based approach with real world measurements [13]. The noise power at the receiver is modeled as thermal noise $\sigma_n^2 = kT_aB$ where k is the Boltzman's constant, T_a is the antenna noise temperature.

TABLE III
Troposcatter Communication Parameters

Parameter	Value	Unit
Horizontal distance (d)	150	km
Transmitter height (h_t)	27	m
Receiver height (h_r)	27	m
Distance between obstacle to TX/RX ($d_{1,2}$)	21	km
Height of obstacles ($h_{1,2}$)	41	m
Transmit power (P_t)	1	kW
Antenna gains ($G_{t,r}$)	41.5	dBi
Antenna noise temperature (T_a)	290	K
Antenna diameters (D_{ant})	3	m

B. Simulation Results

The channel parameters that are used in our simulations can be found in Table III. 1000 atmospheric measurements are used to estimate SNR_{av} in (25) by using proposed ray-based approach, and 1000 realization for complex Gaussian channel matrix $\mathbf{G}$ in (24) are performed for each measurement instant. Therefore, the total of 1 million realization is performed for each capacity results presented by using MATLAB simulations.

Cumulative distribution function (CDF) of capacity in 2×2 MIMO troposcatter link as a function of carrier frequency presented in Fig. 9(a). Due to higher transmission-loss in higher frequencies, capacity decrease with increasing carrier frequency as expected. In addition, CDF of capacity for SISO, SIMO and MIMO employments for 4.7 GHz and 150 km presented in Fig. 9(b). Both reliability and capacity of the link are increased with MIMO employments. As the correlation coefficient increase, the capacity gain is reduced. Increase in the number of receivers without changing the number of transmitters can increase achievable capacity as well. Lastly, MIMO systems also decreases the span of achievable data rates, so that the link becomes more reliable.

Despite of the high losses that are introduced in troposcatter communications, SISO b-LoS troposcatter communication can provide high data rates more than 10 Mbps at 90% of the time for 1 MHz bandwidth. With the partially correlated ($\rho = 0.5$) MIMO employments the link can provide more than 10 Mbps at all times as in Fig. 9(b). Therefore, our analysis show that troposcatter communication can be utilized for high data rate b-LoS applications with high availability.

IX. Conclusion

In this paper, we developed a ray-based channel modeling approach to analyze the transmission-loss, coherence bandwidth,

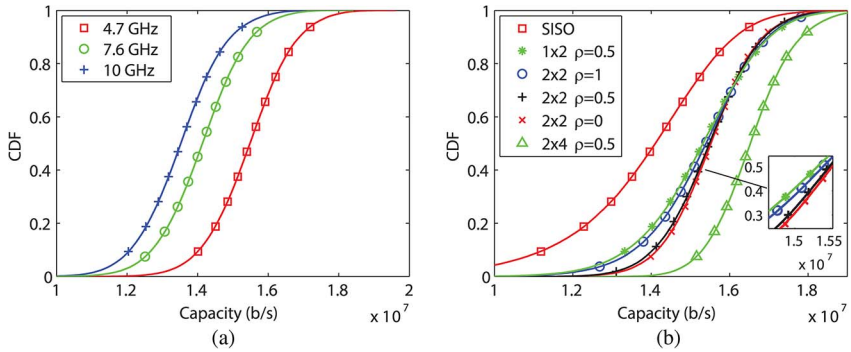

Fig. 9. Capacity of CDF for different frequencies and antennas sizes for troposcatter communication. (a) For different frequencies 2×2, $\rho = 0.5$, 150 km. (b) SISO and MIMO for 4.7 GHz, 150 km.

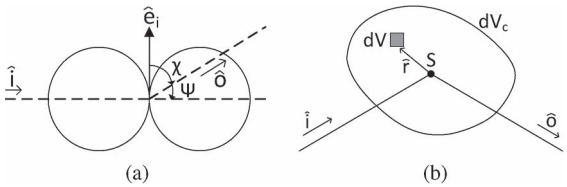

Fig. 10. (a) Radiation pattern for Rayleigh scattering and, (b) Unit scattering common volume.

RMS delay spread and vertical correlation in b-LoS troposcatter links for the first time. We also show that our proposed approach can be used in different climate regions with the required meteorological inputs. According to our results, the troposcatter communication can be used in b-LoS applications up to 300 km. In addition, the b-LoS troposcatter communication can provide high data rates with high availability rates. For these reasons, the troposcatter communication can be used as a communication medium for b-LoS applications which require high data rates and reliability.

Appendix A
The Scattering Cross-Section Calculations

The Rayleigh scattering is valid for the scattering by the atmospheric turbulence because the scattering particles are much lower compared to the wavelength between 4.7–10 GHz range. Beyond this frequency range, the Rayleigh scattering theory deviates from the real world values as reported in ITU-R-R P.452 [17]. Since the modern troposcatter equipments generally operate on 4.4–5 GHz [1], we focus on 1–10 GHz frequency range.

The derivations for the scattering cross-section are mostly taken from [10]. The scattering cross-section for a unit volume is given by

$$\sigma(\hat{\mathbf{o}}, \hat{\mathbf{i}}) = \left| f(\hat{\mathbf{o}}, \hat{\mathbf{i}}) \right|^2 \Big/ dV_c, \tag{27}$$

where $f(\hat{\mathbf{o}}, \hat{\mathbf{i}})$ is the scattering amplitude for the incoming ray $\hat{\mathbf{i}}$ and the scattered ray $\hat{\mathbf{o}}$ as seen in Fig. 10(a). dV_c is the unit volume.

The scattering amplitude for Rayleigh scattering approximation is given by [10]

$$f(\hat{\mathbf{o}}, \hat{\mathbf{i}}) = \frac{k^2}{4\pi} \int_{dV_c} \{-\hat{\mathbf{o}} \times [\hat{\mathbf{o}} \times E(\hat{\mathbf{r}})]\}\, \epsilon(\hat{\mathbf{r}}) \exp(-ik\hat{\mathbf{r}}.\hat{\mathbf{o}}) dV, \tag{28}$$

where $\times$ is the cross product,. is the dot product, $k = 2\pi/\lambda$ is the wavenumber, $\epsilon(\hat{\mathbf{r}})$ is the permittivity at $\hat{\mathbf{r}}$, and $E(\hat{\mathbf{r}})$ is the field at $\hat{\mathbf{r}}$ as seen in Fig. 10(b).

Since the permittivity fluctuations is small for the atmospheric turbulences, we use the Born approximation [10]. In this way, $E(\hat{\mathbf{r}}) = \hat{\mathbf{e}}_i \exp(ik\hat{\mathbf{i}}.\hat{\mathbf{r}})$, where $\hat{\mathbf{i}}$ is the polarization of the incident ray. Then, the scattering amplitude is simplified as

$$f(\hat{\mathbf{o}}, \hat{\mathbf{i}}) = \hat{\mathbf{o}} \sin(\chi) \frac{k^2}{4\pi} \int_{dV_c} \epsilon(\hat{\mathbf{r}}) \exp(i\hat{\mathbf{k}}_s \hat{\mathbf{r}}) dV, \tag{29}$$

where $\sin(\chi) = \{-\hat{\mathbf{o}} \times [\hat{\mathbf{o}} \times \hat{\mathbf{e}}_i]\}$, χ is the angle between the polarization $\hat{\mathbf{e}}_i$ as in Fig. 10(a). $\hat{\mathbf{k}}_s = k(\hat{\mathbf{i}} - \hat{\mathbf{o}})$ with magnitude $k_s = 2k \sin(\Psi/2)$, where Ψ is the scattering angle as seen in Fig. 10(a). In this model, we use linear polarization at the both of the antennas. Therefore, the polarization of the incoming ray is always on the $\hat{\mathbf{e}}_i$ vector, and we can assume that $\sin(\chi) = \cos(\Psi)$.

By combining (27) and (29), the scattering cross-section is given as

$$\sigma(\hat{\mathbf{o}}, \hat{\mathbf{i}}) = \frac{k^4 \cos(\theta)^2}{(4\pi)^2 dV_c} \int_{dV_c} \int_{dV_c} B_n(r_d) \exp\left[i\hat{\mathbf{k}}_s.(\hat{\mathbf{r}}_1 - \hat{\mathbf{r}}_2) \right] dV_1 dV_2, \tag{30}$$

where $B_n(r_d) = \langle \epsilon(\hat{\mathbf{r}}_1)\epsilon(\hat{\mathbf{r}}_2) \rangle / 4$, and $r_d = |\hat{\mathbf{r}}_1 - \hat{\mathbf{r}}_2|$.

Since the correlation distance for $B_n(r_d)$ is much smaller compared to the dimensions of the unit volume dV_c, we can simplify the double integral term in (30) as [10]

$$\int_{dV_c} \int_{dV_c} B_n(r_d) \exp\left[i\hat{\mathbf{k}}_s.(\hat{\mathbf{r}}_1 - \hat{\mathbf{r}}_2) \right] dV_1 dV_2 = \int_{dV_c} dV_1 \int_{\infty} B_n(r_d) \exp[i\hat{\mathbf{k}}_s.\hat{\mathbf{r}}_d] dV_2. \tag{31}$$

In this way, the inside integral in (31) becomes the spectral density of the turbulence which is given as

$$\Phi(k_s) = \left(\frac{1}{2\pi}\right)^3 \int_{\infty} B_n(r_d) \exp[i\hat{\mathbf{k}}_s.\hat{\mathbf{r}}_d]\, dV. \qquad (32)$$

By combining (30) and (32), the scattering cross-section is represented as

$$\sigma(\hat{\mathbf{o}}, \hat{\mathbf{i}}) = \frac{2\pi k^4 \cos(\theta)^2}{dV_c} \int_{dV_c} \Phi(k_s) dV. \qquad (33)$$

We model $\Phi(k_s)$ with the Kolmogorov spectrum technique which assumes the turbulence locally homogeneous [10]. Therefore, the spectrum characteristics becomes constant at the unit volume dV_c, and the scattering cross-section is further simplified as

$$\sigma(\hat{\mathbf{o}}, \hat{\mathbf{i}}) = 2\pi k^4 \cos(\theta)^2 \Phi(k_s). \qquad (34)$$

In our model, we represent the scattering cross-section as a function of α, β and n because the directions are found with the angles in our approach. In the same way, the Kolmogorov spectrum is represented with $\Phi(\alpha, \beta, n)$.

REFERENCES

[1] "Introduction to troposcatter communications: A brief synopsis of over-the-horizon troposcatter," Comtech Syst., Tech. Inf., Orlando, FL, USA. [Online]. Available: http://www.comtechsystems.com/wp-content/uploads/2014/05/Troposcatter-Introduction-Nov-2013.pdf

[2] Troposcatter Hardware, Comtech Systems, Oct. 2014. [Online]. Available: http://www.comtechsystems.com/products-systems/troposcatter-hardware/

[3] Troposcatter, General Dynamics SATCOM Technologies, Oct. 2014. [Online]. Available: http://www.gdsatcom.com/troposcatter.php.

[4] G. Roda, *Troposcatter Radio Links*. Norwood, MA, USA: Artech House, 1988.

[5] "Propagation Prediction Techniques and Data Required for the Design of Trans-Horizon Radio-Relay Systems," Int. Telecommun. Union (ITU-R), Geneva, Switzerland, Rec. P.617-3, 2013.

[6] P. Bello, "A troposcatter channel model," *IEEE Trans. Commun. Technol.*, vol. 17, no. 2, pp. 130–137, Apr. 1969.

[7] Z. Yu and C. Xi-hong, "Research on MRC based on Rake receiver in troposcatter communication," in *Proc. Consum. Electron., Commun. Netw.*, 2011, pp. 4342–4345.

[8] Y. Wang, Y. Fang, X. Da, and W. Jin, "Study on modeling of troposcatter communication and MRC in correlated channel by Matlab," in *Proc. Wireless Commun., Netw. Mobile Comput.*, 2008, pp. 1–4.

[9] E. Dinc and O. B. Akan, "A ray-based channel model for MIMO troposcatter communications," *Proc. IEEE PIMRC*, London, U.K., Sep. 2013, pp. 243–247.

[10] A. Ishimaru, *Wave Propagation and Scattering in Random Media*. New York, NY, USA: Wiley, 1999.

[11] L. Tsang, J. A. Kong, and K. Ding, *Scattering of Electromagnetic Waves: Theories and Applications*. New York, NY, USA: Wiley, 2000.

[12] F. S. Marzano and G. D'Auria, "Model-based prediction of amplitude scintillation variance due to clear-air tropospheric turbulence on Earth-satellite microwave links," *IEEE Trans. Antennas Propag.*, vol. 46, no. 10, pp. 1506–1518, Oct. 1998.

[13] "NAMMA Lidar Atmospheric Sensing Experiment (LASE)," Nat. Aeronautics Space Admin. (NASA) EOSDIS GHRC DAAC, Washington, DC, USA, Jan. 30, 2013. [Online]. Available: http://ghrc.msfc.nasa.gov/index.html

[14] M. W. Gough and G. C. Rider, "Angle diversity in troposcatter communications. Some confirmatory trials," *Proc. Inst. Elect. Eng.*, vol. 122, no. 7, pp. 713–719, Jul. 1975.

[15] R. W. Meadows, "Tropospheric scatter observations at 3 480 Mc/s with aerials of variable spacing," in *Proc. Inst. Elect. Eng.*, vol. 108, no. 40, pp. 349–360, Jul. 1961.

[16] S. Zhou, S. Xu, and L. Quan, "Analysis on performance of MIMO channel estimation in troposcatter communication," *Proc. 54th Res. Instit. CETC*, Shijiazhuang, China, 2011.

[17] "Prediction Procedure for the Evaluation of Interference Between Stations on the Surface of the Earth at Frequencies Above About 0.1 GHz," Int. Telecommun. Union (ITU-R), Geneva, Switzerland, Rec. P.452-15, 2013.

[18] "The Radio Refractive Index: Its Formula and Refractivity Data," Int. Telecommun. Union (ITU-R), Geneva, Switzerland, Rec. P.453-10, 2012.

[19] D. M. J. Devasirvatham, "Effects of atmospheric turbulence on microwave and millimeter wave satellite communications systems," Ph.D. dissertation, Ohio State Univ., Columbus, OH, USA, May 1981.

[20] H. Vasseur, "Prediction of tropospheric scintillation on satellite links from radiosonde data," *IEEE Trans. Antennas Propag.*, vol. 47, no. 2, pp. 293–301, Feb. 1999.

[21] A. Ludi and A. Magun, "Near-horizontal line-of-sight millimeter-wave propagation measurements for the determination of outer length scales and anisotropy of turbulent refractive index fluctuations in the lower troposphere," *Radio Sci.*, vol. 37, no. 2, 2002, pp. 10–18.

[22] G. Ehret, C. Kiemle, W. Renger, and G. Simmet, "Airborne remote sensing of tropospheric water vapor with a near-infrared differential absorption lidar system," *Appl. Opt.*, vol. 32, no. 24, pp. 4534–4551, Aug. 1993.

[23] R. W. McMillan, "Intensity and angle-of-arrival effects on microwave propagation caused by atmospheric turbulence," in *Proc. IEEE COMCAS*, May 2008, pp. 1–10.

[24] S. D. Burk, "Refractive index structure parameters: Time-dependent calculations using a numerical boundary-layer model," *J. Appl. Meteor.*, vol. 19, no. 5, pp. 562–576, May 1980.

[25] E. Dinc and O. B. Akan, "Beyond-line-of-sight communications with ducting layer," *IEEE Commun. Mag.*, vol. 52, no. 10, pp. 37–43, Oct. 2014.

[26] L. Bastos and H. Wietgrefe, "Tactical troposcatter applications in challenging climate zones," in *Proc. IEEE MILCOM*, 2012, pp. 1–6.

[27] "Troposcatter Modem," General Dynamics, Falls Church, VA, USA, Model TM-20 datasheet, Oct. 2008.

[28] S. Da-shan, G. J. Foschini, M. J. Gans, and J. M. Kahn, "Fading correlation and its effect on the capacity of multielement antenna systems," *IEEE Trans. Commun.*, vol. 48, no. 3, pp. 502–513, Mar. 2000.

[29] P. Kyritsi and D. C. Cox, "Effect of element polarization on the capacity of a MIMO system," in *Proc. IEEE WCNC*, Mar. 2002, vol. 2, pp. 892–896.

[30] D. Gesbert, H. Bolcskei, D. Gore, and A. Paulraj, "MIMO wireless channels: Capacity and performance prediction," in *Proc. IEEE GLOBECOM*, 2000, vol. 2, pp. 1083–1088.

[31] A. Goldsmith, *Wireless Communications*. Cambridge, U.K.: Cambridge Univ. Press, 2005.

[32] K. Yu *et al.*, "Second order statistics of NLOS indoor MIMO channels based on 5.2 GHz measurements," in *Proc. IEEE GLOBECOM*, 2001, vol. 1, pp. 156–160.

Ergin Dinc (S'12) received the B.Sc. degree in electrical and electronics engineering from Bogazici University, Istanbul, Turkey, in 2012. He is currently a Research Assistant at Next-generation and Wireless Communications Laboratory (NWCL) and pursuing the Ph.D. degree at the Electrical and Electronics Engineering Department, Koc University, Istanbul, Turkey. His current research interests include communication theory, beyond-Line-of-Sight (b-LoS) communications with troposcatter and atmospheric ducts.

Ozgur B. Akan (M'00–SM'07) received the Ph.D. degree in electrical and computer engineering from the Broadband and Wireless Networking Laboratory, School of Electrical and Computer Engineering, Georgia Institute of Technology, USA, in 2004. He is currently a Full Professor with the Department of Electrical and Electronics Engineering, Koc University and the Director of the Next-generation and Wireless Communications Laboratory. His current research interests are in wireless communications, nano-scale and molecular communications, and information theory. He is an Associate Editor of the IEEE TRANSACTIONS ON COMMUNICATIONS, the IEEE TRANSACTIONS ON VEHICULAR TECHNOLOGY, the *International Journal of Communication Systems* (Wiley), *Nano Communication Networks* (Elsevier), and *European Transactions on Technology*.